NANO · MICRO small
www.small-journal.com

Water-Stabilized Vanadyl Phosphate Monohydrate Ultrathin Nanosheets toward High Voltage Al-Ion Batteries

*Jiening Zheng, Tian Xu, Guanglin Xia, Wen-Gang Cui, Yaxiong Yang, and Xuebin Yu**

Al ion batteries (AIBs) are attracting considerable attention owing to high volumetric capacity, low cost, and high safety. However, the strong electrostatic interaction between Al^{3+} and host lattice leads to discontented cycling life and inferior rate capability. Herein, a new strategy of employing water molecules contained $VOPO_4{\cdot}H_2O$ to boost Al^{3+} migration via the charge shielding effect of water is reported. It is revealed that $VOPO_4{\cdot}H_2O$ with water lubrication effect and smaller steric hindrance owns high capacity and fast Al^{3+} diffusion, while the loss of unstable water upon cycling leads to a rapid performance degradation. To address this problem, ultrathin $VOPO_4{\cdot}H_2O$@MXene nanosheets are fabricated via the formed Ti—O—V bond between $VOPO_4{\cdot}H_2O$ and MXene. The MXene aided exfoliation results in enhanced $V—O_{water}$ bond strength between H_2O and $VOPO_4$ that endows the obtained composite with strong water holding ability, contributing to the extraordinary cycling stability. Consequently, the $VOPO_4{\cdot}H_2O$@MXene delivers a high discharge potential of 1.8 V and maintains discharge capacities of 410 and 374.8 mAh g^{-1} after 420 and 2000 cycles at the current densities of 0.5 and 1.0 A g^{-1}, respectively. This work provides a new understanding of water-contained AIBs cathodes and vital guidance for developing high-performance AIBs.

1. Introduction

The requirements for rechargeable batteries with higher theoretical energy density, lower cost, and sustainability than the market dominated lithium ion batteries (LIBs) inspires further research enthusiasm to the development of post-LIBs systems.[1] Rechargeable batteries involving multivalent-ion (e.g., Mg^{2+}, Zn^{2+}, Al^{3+}, Ca^{2+}) shuttling represent one of the promising successors and are envisioned to surpass the energy density of LIBs.[2] As the most abundant metallic element, Al has received growing attention due to its high capacity, low cost, high safety, easy operation, and environmental benignity.[3] Therefore, Al ion batteries (AIBs) have been regarded as attractive energy storage system, which would propel the substantial development of the energy storage technology.[4] In order to design high energy density storage devices, the identifying of host materials with high performance, especially elevated work potential, is essential. Due to the high electronegativity of oxygen, the metal oxides own strong ionic chemical bonds, which consequently result in increased plateau voltages.[5] Examples of such oxides owning potential high discharge voltages are amorphous V_2O_5 (≈0.9 V),[6] MoO_2 (1.9 V),[7] TiO_2 (≈1.0 V)[8] and so on. Despite their advantage in working potential, they usually suffer from low capacity, discontented cycling life, and inferior rate capability, which originate from the slow reaction kinetics caused by the strong Coulombic interaction between the trivalent Al^{3+} and oxide host lattice.[9]

Previous researches have demonstrated that water molecules can be applied as "lubricant" to facilitate ions diffusion.[10] Typically, vanadyl phosphate dihydrate ($VOPO_4 \cdot 2H_2O$) with a long intercalation chemistry history, has been recently developed as a potential cathode material for various alkali metal-ion batteries, meriting from its high redox reaction potential due to the strong inductive effect of [PO_4] tetrahedrons and the large interlayer space stemming from the interlayer water molecules.[11] Moreover, the easier multivalent ions (Mg^{2+} and Zn^{2+}) intercalation into $VOPO_4 \cdot 2H_2O$ can take place with the aid of the water molecules.[11e,12] The study of vanadyl phosphate hydrate as AIBs cathode was first reported in 2020 by Wang and co-workers via fabricating a $VOPO_4$-graphene heterostructure.[11f] Although an improved cycling performance originating from its zero-strain property is achieved, the potential high discharge plateau voltage and capacity of vanadyl phosphate hydrate are underutilized. In addition, the effect and mechanism of the bonded water molecule content and its stability on the aluminum storage behavior have not been systematically studied.

In this work, we select $VOPO_4 \cdot 2H_2O$ as a model cathode to reveal its Al^{3+} storage behaviors. As expected, the $VOPO_4 \cdot 2H_2O$ presents high discharge plateau and holds high potential Al^{3+} storage capacity. We further investigate the relationship between water content and electrochemical performance. Interestingly, our density functional theory (DFT) calculations results reveal that, compared with $VOPO_4 \cdot 2H_2O$ and $VOPO_4$, the $VOPO_4 \cdot H_2O$ possesses the lowest Al^{3+} diffusion barrier and

J. Zheng, T. Xu, G. Xia, X. Yu
Department of Materials Science
Fudan University
Shanghai 200433, China
E-mail: yuxuebin@fudan.edu.cn
W.-G. Cui, Y. Yang
Institute of Science and Technology for New Energy
Xi'an Technological University
Xi'an 710021, China
The ORCID identification number(s) for the author(s) of this article can be found under https://doi.org/10.1002/smll.202207619.

DOI: 10.1002/smll.202207619

adsorption energy, which are unsurprisingly validated by the enhanced Al^{3+} storage performance. Although $VOPO_4 \cdot H_2O$ is shown to be the most attractive cathode material, it suffers from inevitably capacity loss during continuous cycling, resulted from the structural and composition changes of $VOPO_4 \cdot H_2O$ upon cycling. Besides, the $VOPO_4 \cdot H_2O$ is sensitive to the moisture in the air and can easily transfer to $VOPO_4 \cdot 2H_2O$. These obstacles motivate us to find an effective strategy to obtain $VOPO_4 \cdot H_2O$ with high stability and insensitivity.

It is well known that the surfaces of MXenes are terminated with numerous hydrophilic groups (named as T), such as −OH, −O, and −F, which can effectively bind with other materials through the formation of definite interactions, such as M−O−Ti (M = metal atoms), hydrogen bonding, and so on.[13] This fancy property of MXene is expected to effectively trigger the hydrogen bonds fracture of the interlayer water in $VOPO_4 \cdot 2H_2O$ and leads to the escape of part of water molecules. Hence, heterostructured $VOPO_4 \cdot H_2O$@MXene composite was fabricated by a simple mechanical stirring of bulk $VOPO_4 \cdot 2H_2O$ and MXene mixture. This MXene aided stripping strategy can exfoliate the bulk $VOPO_4 \cdot 2H_2O$ thoroughly and remove partial water molecules. Notably, the enhanced stripping degree induced by MXene facilitates the formation of rich oxygen vacancies, resulting in the shortened $V-O_{water}$ bonds that are confirmed by the DFT calculations. This ingenious design contributes to the significant improvement on the stability of water molecules in $VOPO_4 \cdot H_2O$@MXene, which is ascertained by its obvious water loss hysteresis. Consequently, the $VOPO_4 \cdot H_2O$@MXene delivers high voltage plateau with tiny polarization, high reversible discharge capacity with long cycle life and favorable rate capability.

2. Results and Discussion

2.1. Synthesis, Characterization, and Electrochemical Tests of $VOPO_4 \cdot nH_2O$ (n = 0, 1, 2)

Figure 1a exhibits the X-ray diffraction (XRD) pattern of $VOPO_4 \cdot 2H_2O$. All of the peaks can be indexed to $VOPO_4 \cdot 2H_2O$ (JCPDS No. 36-1472) with P4/n space group. The main (001) peak is located at 11.9°, reflecting that $VOPO_4 \cdot 2H_2O$ owns a large interlayer spacing of 0.74 nm. As displayed in the schematic structure (inset in Figure 1a), $VOPO_4 \cdot 2H_2O$ has the typical layered crystal structure consisting of vertex-sharing VO_6 octahedra linking to phosphate PO_4 tetrahedra with a ratio of 1:1. Between the $VOPO_4$ layer, one water molecule (called structural water) coordinates with the layer through the V−O

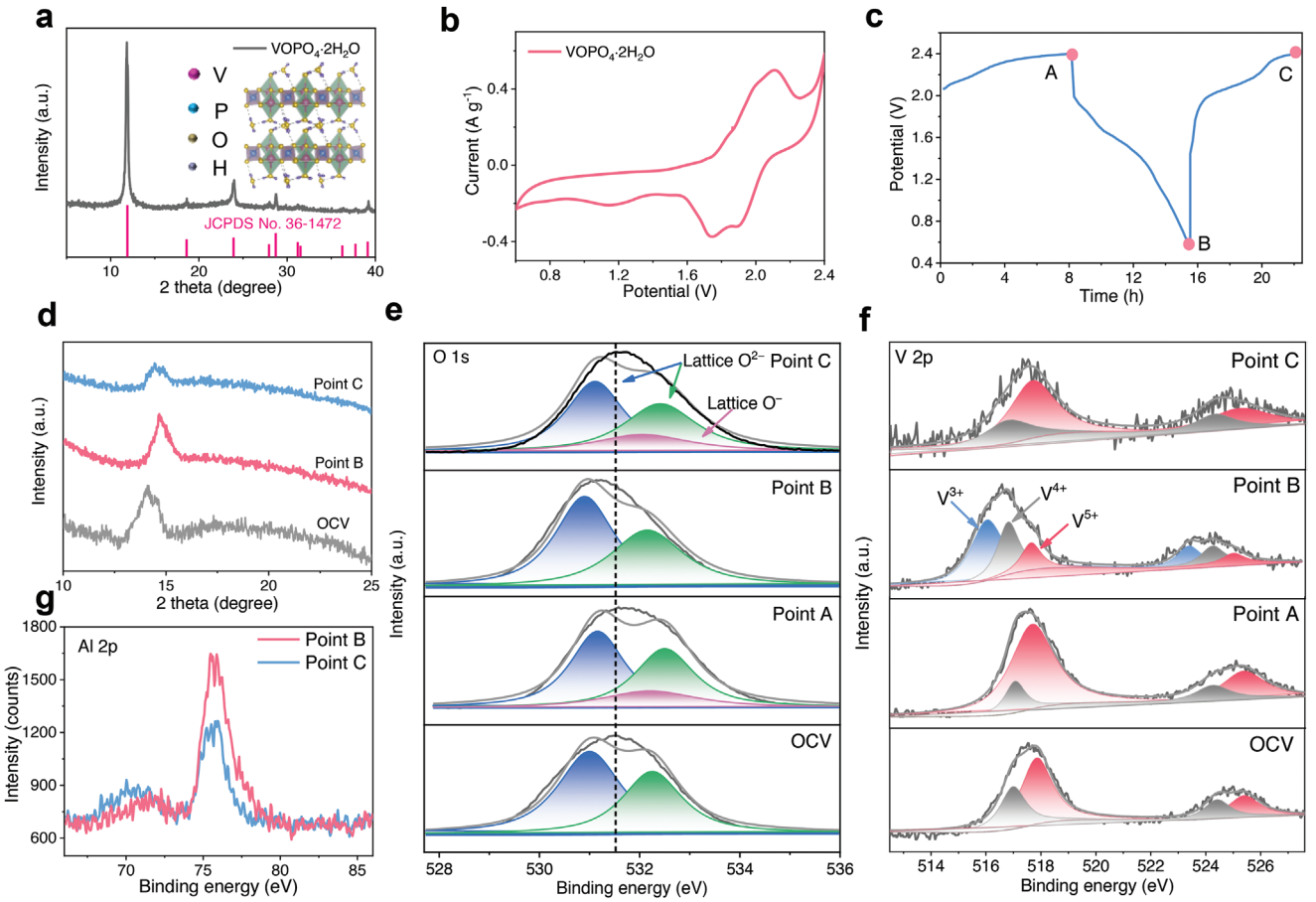

Figure 1. a) XRD pattern of $VOPO_4 \cdot 2H_2O$. Inset: crystal structure of $VOPO_4 \cdot 2H_2O$. b) CV curve of $VOPO_4 \cdot 2H_2O$ acquired at 0.5 mV s^{-1}. c) Galvanostatic charge and discharge curve of $VOPO_4 \cdot 2H_2O$. d) XRD patterns, and ex situ XPS results of e) O 1s, f) V 2p, and g) Al 2p of $VOPO_4 \cdot 2H_2O$ cathode at different reaction states.

bond and the other (called crystal water) connects neighboring layers together via the weak hydrogen bonds.[11c] The regularly arrayed discrete spots in the selected area electron diffraction (SAED) pattern demonstrate the top-quality single crystalline property of $VOPO_4 \cdot 2H_2O$ (Figure S1a, Supporting Information). The lattice distance extracted from the high resolution transmission electron microscopy (HRTEM) image of the selected area is about 0.31 nm, which is assigned to (200) crystal plane (Figure S1b, Supporting Information), matching well with the SAED pattern. Cyclic voltammetry (CV) measurement was implemented to investigate the fundamental redox reactions for $VOPO_4 \cdot 2H_2O$ (Figure 1b). A pair of distinct redox peaks appearing at high potential of 2.11/1.90 V can be observed in the initial cycle at the scan rate of 0.5 mV s^{-1}, followed by two pairs of peaks at 1.99/1.75 and 1.60/1.14 V, respectively, revealing the reversible redox reaction process of active sites. Figure S2 (Supporting Information) summarizes the discharge voltages of different kinds of materials, and the discharge potential of $VOPO_4 \cdot 2H_2O$ is higher than most of the reported AIBs cathode materials, indicating a great potential for achieving high energy density. To elucidate the aluminum storage/release mechanism during the redox reaction process, ex situ XRD and X-ray photoelectron spectroscopy (XPS) tests were conducted at different terminated voltage stages as illustrated in Figure 1c. As witnessed in the XRD patterns (Figure 1d), the (001) peak shifts to higher degree along with the decrease of the interlayer distance upon discharging, which is ascribed to the strong electrostatic interaction between the inserted Al^{3+} and the O atoms in the $VOPO_4 \cdot 2H_2O$.[14] During charging, the (001) peak reversibly returns back to the lower degree but not to that of the original electrode, indicative of the trapping of some Al^{3+} ions in the lattice.[11e] No impurity diffraction peaks arise in the XRD results, suggestive of a typical intercalation/deintercalation mechanism for Al^{3+} storage in the $VOPO_4 \cdot 2H_2O$. Besides, compared with the $VOPO_4 \cdot 2H_2O$ powder, the $VOPO_4 \cdot 2H_2O$ casted Mo foil cathode displays a right (001) peak shift (Figure S3, Supporting Information). This shift has also been observed in other literatures.[15] Ex situ XPS spectra of O 1s illustrated in Figure 1e indicate that the O 1s spectrum of pristine $VOPO_4 \cdot 2H_2O$ owns two characteristic peaks at 531.0 and 532.3 eV, assigning to the binding energies of lattice O^{2-}.[16] For the V 2p spectrum of pristine $VOPO_4 \cdot 2H_2O$ (Figure 1f), two pairs of peaks located at 517.9/525.5 and 517.0/524.4 eV are pointed to V^{5+} and V^{4+}, respectively.[11d] By charging to 2.4 V (point A), a new peak of O^- appears at around 532.0 eV, indicating that O^{2-} is oxidized to O^- during the charging process.[17] However, the V 2p spectrum remains almost unchanged after fully charged (point A). After fully discharged (point B), the new peak of O^- disappears, demonstrating that the change of chemical states of the oxygen is reversible. While for V 2p spectrum at this state (point B), a new peak of V^{3+} appears at the expense of the V^{5+} peak intensity, reflecting the reduction of V^{5+} due to the Al^{3+} insertion. Those observations uncover that the discharge capacity of the $VOPO_4 \cdot 2H_2O$ stems from the simultaneous redox reactions of oxygen and vanadium. At the charged state of 2nd cycle (point C), the O 1s and V 2p spectra keep similar to those of the 1st charged cathode, further confirming the high reversibility of oxygen and vanadium redox process. In addition, the XPS spectra of Al 2p confirm the insertion of Al^{3+} with the stronger Al signal at fully discharged state than that at fully charged state (Figure 1g). The Al signal still exists at the fully charged state, which is due to the trapped Al^{3+} in the $VOPO_4 \cdot 2H_2O$ lattice. Clearly, the introduction of oxygen redox process improves the average operating voltage and capacity of the AIBs, thus resulting in enhanced energy density.[18]

To study the effect of water content on the Al^{3+} storage properties, a series of $VOPO_4 \cdot nH_2O$ with different water contents (n = 0, 1, 2) were prepared. The thermogravimetric analysis (TGA) curve (**Figure 2**a) demonstrates that the crystal water of $VOPO_4 \cdot 2H_2O$ escapes starting at around 50 °C followed by the complete loss at about 147 °C. Based on the loss temperature of crystal water, the anhydrous $VOPO_4$ was prepared through vacuum heating of $VOPO_4 \cdot 2H_2O$ at 150 °C for 2 h and the $VOPO_4 \cdot H_2O$ was synthesized via heating $VOPO_4 \cdot 2H_2O$ slowly under vacuum followed by immediate stop at 75 °C (Figure S4, Supporting Information). The XRD patterns of $VOPO_4$ and $VOPO_4 \cdot H_2O$ verify their successful preparation (Figure 2b). Specifically, the (001) peak located at 21.2° comes from $VOPO_4$,[11e] while the peak at 14.1° (d = 0.63 nm) originates from $VOPO_4 \cdot H_2O$, which agrees well with the calculated interlayer distance for $VOPO_4 \cdot H_2O$ (6.30 Å).[19] The TGA curve provided in Figure S5 (Supporting Information) shows that the mass of $VOPO_4$ is almost unchanged within room temperature to 600 °C, confirming its successful dehydration. Figure 2c depicts the CV curves of $VOPO_4 \cdot H_2O$ and $VOPO_4$ acquired at 0.5 mV s^{-1}. They display analogous shapes compared with that of $VOPO_4 \cdot 2H_2O$ (Figure 1b), demonstrating their similar Al^{3+} storage mechanism. Notably, the $VOPO_4 \cdot H_2O$ exhibits highest redox peak currents, indicating its outstanding Al^{3+} storage ability. The galvanostatic discharge/charge experiments were conducted to further evaluate the electrochemical behaviors of $VOPO_4 \cdot 2H_2O$, $VOPO_4 \cdot H_2O$, and $VOPO_4$ electrodes.

Their cycling performances at 1.0 A g^{-1} are compared in Figure 2d. Obviously, the $VOPO_4 \cdot H_2O$ harvests the highest initial discharge capacity of 124.8 mAh g^{-1} and the capacity can be maintained stably for a period and then falls gradually. For $VOPO_4 \cdot 2H_2O$ cathode, it delivers a discharge capacity increment and reaches the highest value of 134.9 mAh g^{-1} at the 220th cycle. Since then, its capacity declines gradually. Meanwhile, the $VOPO_4$ always keeps stable discharge capacity with lowest value during the whole cycle process. We conducted a series of experiments to ascertain the reasons of the capacity fading and the results show that the active material dissolution, self-discharge phenomenon, and structure damage can be excluded (Figures S6–S8, Supporting Information). Hence, we speculate that the capacity decrease of $VOPO_4 \cdot 2H_2O$ and $VOPO_4 \cdot H_2O$ may be caused by the escape of H_2O molecules among the deep discharge/charge cycle as the H_2O molecules are beneficial for multivalent ions storage.[10b,11c] The XRD pattern of the $VOPO_4 \cdot 2H_2O$ after cycles is shown in Figure S9 (Supporting Information). Compared with the original sample, the cycled $VOPO_4 \cdot 2H_2O$ displays a discernible (001) peak right shift, which is due to the escape of the water or the irreversible insertion of Al^{3+}.[20] Therefore, the TGA was conducted to figure out the water contents before and after cycling. As displayed in Figure 2e, it can be clearly observed for the decreased water content in the cycled $VOPO_4 \cdot 2H_2O$, corroborating the

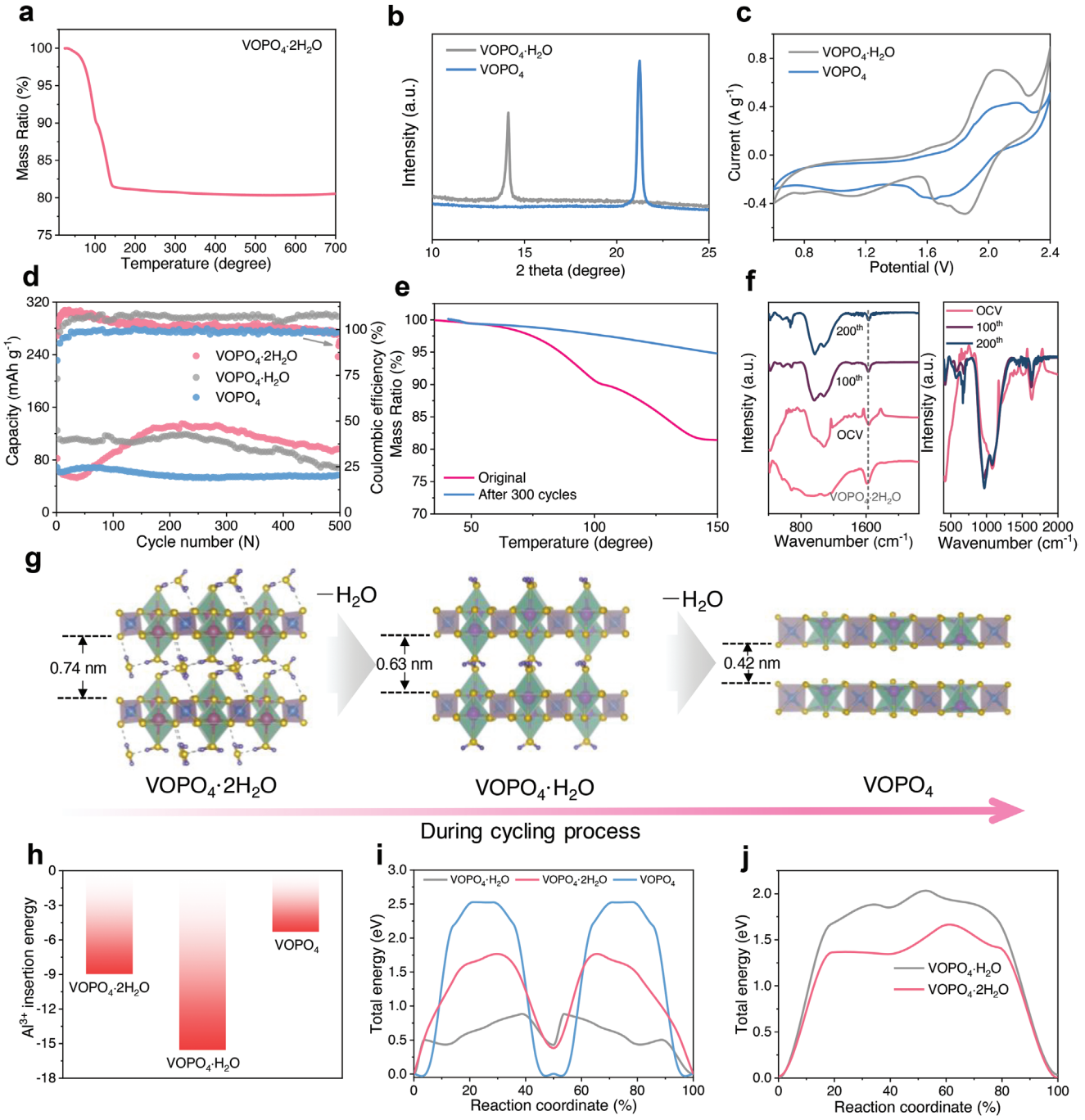

Figure 2. a) The TGA curves of $VOPO_4{\cdot}2H_2O$. b) The XRD patterns and c) CV curves of $VOPO_4{\cdot}H_2O$ and $VOPO_4$. d) Cycling performance and Coulombic efficiency of $VOPO_4{\cdot}2H_2O$, $VOPO_4{\cdot}H_2O$, and $VOPO_4$ at 1.0 A g^{-1}. e) The TGA curves of pristine $VOPO_4{\cdot}2H_2O$ sample and cycled $VOPO_4{\cdot}2H_2O$ cathode. f) The FTIR curves of $VOPO_4{\cdot}2H_2O$ during cycling process. g) Schematic diagram of structural change of $VOPO_4{\cdot}2H_2O$ upon successive Al^{3+} insertion/deinsertion. Color modes: red sphere for V, yellow sphere for O, blue sphere for P, and purple sphere for H, respectively. h) Corresponding Al^{3+} insertion energies in these composites. i) The energy curves of $VOPO_4{\cdot}2H_2O$, $VOPO_4{\cdot}H_2O$, and $VOPO_4$ during the Al^{3+} migration process. j) The curves of energy variation in water loss process of $VOPO_4{\cdot}2H_2O$ and $VOPO_4{\cdot}H_2O$.

water escape during cycling. Additionally, the Fourier transform infrared spectroscopy (FTIR) further witnesses the water deinsertion judging via the weakened absorption band at around 1615 cm^{-1} corresponding to the vibration of water molecules (Figure 2f). Based on the above analysis, Figure 2g generalizes the phase conversion process of $VOPO_4{\cdot}2H_2O$ during repeated Al^{3+} insertion/deinsertion cycles, i.e., $VOPO_4{\cdot}2H_2O \rightarrow VOPO_4{\cdot}H_2O \rightarrow VOPO_4$ due to the gradual water loss during cycling.

Given that the performances of these electrodes can be summarized as the following order: $VOPO_4{\cdot}H_2O$ > $VOPO_4{\cdot}2H_2O$ > $VOPO_4$, we infer that the water content plays a crucial role

in determining the electrochemical properties. In order to understand the relationship between the water content and the electrochemical performance of $VOPO_4 \cdot nH_2O$ (n = 0, 1, 2), DFT calculations of the Al^{3+} insertion energies on these compounds were first performed. Figure S10a–c (Supporting Information) show the aluminum ion adsorption models for the $VOPO_4 \cdot nH_2O$ (n = 0, 1, 2) cathodes. As presented in Figure 2h, the Al^{3+} insertion energy on the hydrates of $VOPO_4 \cdot 2H_2O$ (–8.97 eV) and $VOPO_4 \cdot H_2O$ (–15.56 eV) is lower than that on the anhydrous $VOPO_4$ (–5.20 eV), suggesting that the water molecules can facilitate Al^{3+} insertion process originating from its effective Al^{3+} charge shielding role.[21] Notably, although the $VOPO_4 \cdot H_2O$ owns less water molecules than $VOPO_4 \cdot 2H_2O$, it exhibits more negative Al^{3+} insertion energy, which can be attributed to the decreased steric hindrance of $VOPO_4 \cdot H_2O$ because of the removal of crystal water. The Al^{3+} diffusion in these compounds was simulated using the CI-NEB method. The possible Al^{3+} migration paths in $VOPO_4 \cdot 2H_2O$, $VOPO_4 \cdot H_2O$, and $VOPO_4$ are given in Figure S10d–f (Supporting Information). In comparison with $VOPO_4 \cdot 2H_2O$ (1.766 eV) and $VOPO_4$ (2.528 eV), the $VOPO_4 \cdot H_2O$ possesses the lowest Al^{3+} diffusion barrier (0.884 eV, Figure 2i). The theoretical calculations rationally confirm the advantages of $VOPO_4 \cdot H_2O$ in regard of Al^{3+} insertion energy and Al^{3+} diffusion energy barrier, and account well for its improved aluminum-storage behaviors toward AIBs. We further calculated the water-holding ability of these compounds. As illustrated in Figure 2j, the $VOPO_4 \cdot H_2O$ displays difficult water migration confirmed by its higher water migration energy (2.03 eV) compared with that of $VOPO_4 \cdot 2H_2O$ (1.66 eV), demonstrating the higher water-holding ability of $VOPO_4 \cdot H_2O$. These results explain well the observations in Figure 2d of the relatively stable cycle performance of $VOPO_4 \cdot H_2O$ than $VOPO_4 \cdot 2H_2O$ in the initial ≈220 cycles, during which the capacity of $VOPO_4 \cdot 2H_2O$ gradually increases. The capacity increment could be attributed to the dehydration process of $VOPO_4 \cdot 2H_2O$, resulting in the formation of $VOPO_4 \cdot H_2O$. Despite of the stronger water-preserving capability of $VOPO_4 \cdot H_2O$, it inevitably suffers from water escape witnessed by the capacity decay after ≈300 cycles.

2.2. Synthesis, Characterization, and Electrochemical Tests of $VOPO_4 \cdot nH_2O$@MXene

In order to obtain water stable $VOPO_4 \cdot H_2O$, the MXene aided synthesis of $VOPO_4 \cdot nH_2O$ with various water contents was conducted and the preparation process is illustrated in **Figure 3**a. Specifically, MXene nanosheets were added dropwise into the bulk $VOPO_4 \cdot 2H_2O$-isopropanol suspension under mild mechanical stirring. Immediately, the multilayered $VOPO_4 \cdot 2H_2O$ were effectively exfoliated into few-layered $VOPO_4 \cdot nH_2O$ nanosheets by the "dragging effect" of MXene nanosheets, leading to the novel ultrathin heterostructured $VOPO_4 \cdot nH_2O$@MXene composite. We synthesized a series of the composites with different MXene contents, which are determined by ICP-OES analysis, accounting for 10%, 12%, 16%, and 48%, respectively (Table S1, Supporting Information). And these composites are denoted as $VOPO_4 \cdot nH_2O$@MXene-10, $VOPO_4 \cdot nH_2O$@MXene-12, $VOPO_4 \cdot nH_2O$@MXene-16, and $VOPO_4 \cdot nH_2O$@MXene-48, respectively. The bulk $VOPO_4 \cdot 2H_2O$ exhibits square layers heavily stacked morphology with lateral size ranging from several to dozens of micrometers before stripping (Figure 3b). Besides, the SEM image of the MXene nanosheets which are ultrasonic exfoliated from the acid etched Ti_3AlC_2 display loose and flexible layered structure with large lateral size (Figure S11a, Supporting Information). The interplanar distance of MXene is 1.26 nm revealed by XRD pattern, which presents the characteristic peak (002) at ≈7.0° (Figure S11b, Supporting Information). Notably, the $VOPO_4 \cdot nH_2O$@MXene exhibits ultrathin layered morphology after hybridization (Figure 3c, using $VOPO_4 \cdot nH_2O$@MXene-12 as an example), revealing the tight contact between $VOPO_4 \cdot nH_2O$ and MXene, thereby leading to effective face-to-face electrical connections. The atomic force microscopy (AFM) characterization also proves the formation of 2D/2D interfacial interaction with the average layered thickness of around 4 nm (Figure 3d). The nearly transparent of the transmission electron microscope (TEM) image (Figure 3e) further uncovers the ultrathin property of the $VOPO_4 \cdot nH_2O$@MXene-12. The HRTEM image (Figure 3f) gives the MXene layer edges distinctly with a distance of ≈2.0 nm between individual layers higher than the calculated interlayer distance of pure MXene (1.26 nm), which could be ascribed to the growth of $VOPO_4$ nanosheets.[22] The SAED pattern exhibits diffraction dots of both $VOPO_4$ and MXene nanosheets, indicative of the hybridization of MXene and $VOPO_4 \cdot nH_2O$ (Figure 3g). The scanning transmission electron microscopy (STEM) image with energy-dispersive X-ray spectroscopy (EDS) mapping in Figure 3h vividly showcase the homogeneous distribution of V, O, P, Ti, and C, corroborating the successful formation of $VOPO_4 \cdot nH_2O$@MXene heterostructure. Besides, the $VOPO_4 \cdot nH_2O$@MXene-10 (Figure S12, Supporting Information), $VOPO_4 \cdot nH_2O$@MXene-16 (Figure S13, Supporting Information), and $VOPO_4 \cdot nH_2O$@MXene-48 (Figure S14, Supporting Information) also show ultrathin layered structure with uniform distributed elements (V, O, P, Ti, C), demonstrating the universality of this developed strategy towards fabrication of ultrathin $VOPO_4 \cdot nH_2O$@MXene heterostructure.

The XRD patterns of $VOPO_4 \cdot nH_2O$@MXene hybrids are displayed in **Figure 4**a. Obviously, the (001) peak of $VOPO_4 \cdot nH_2O$@MXene with 10 wt% MXene shifts from 11.9° of pure $VOPO_4 \cdot 2H_2O$ to 13.6°, along with the decrease of interlayer distance from 0.74 to 0.65 nm, suggesting the removal of water molecules from $VOPO_4 \cdot 2H_2O$ interlayer with the dragging effect of MXene under stirring, which can effectively promote the hydrogen bonds fracture in $VOPO_4 \cdot 2H_2O$. Interestingly, this (001) peak moves toward higher degree with the increase of the MXene amount, revealing that the $VOPO_4 \cdot nH_2O$ with different water contents can be synthesized controllably through simply adjusting MXene amounts. Most notably, the (001) peak position of $VOPO_4 \cdot nH_2O$@MXene-12 (14.0°) is nearest to that of $VOPO_4 \cdot H_2O$ (14.1°) compared with other composites, indicating the successful synthesis of $VOPO_4 \cdot H_2O$@MXene. It is well known that the $VOPO_4 \cdot H_2O$ possessing the (001) peak located at around 14.1° is hard to obtain through common ultrasonic stripping, which usually leads to low stripping degree, validated by the minor (001) diffraction peak right shift (only ≈1°).[23] Therefore, this MXene aided stripping strategy provides a shortcut for the synthesis of $VOPO_4 \cdot H_2O$.

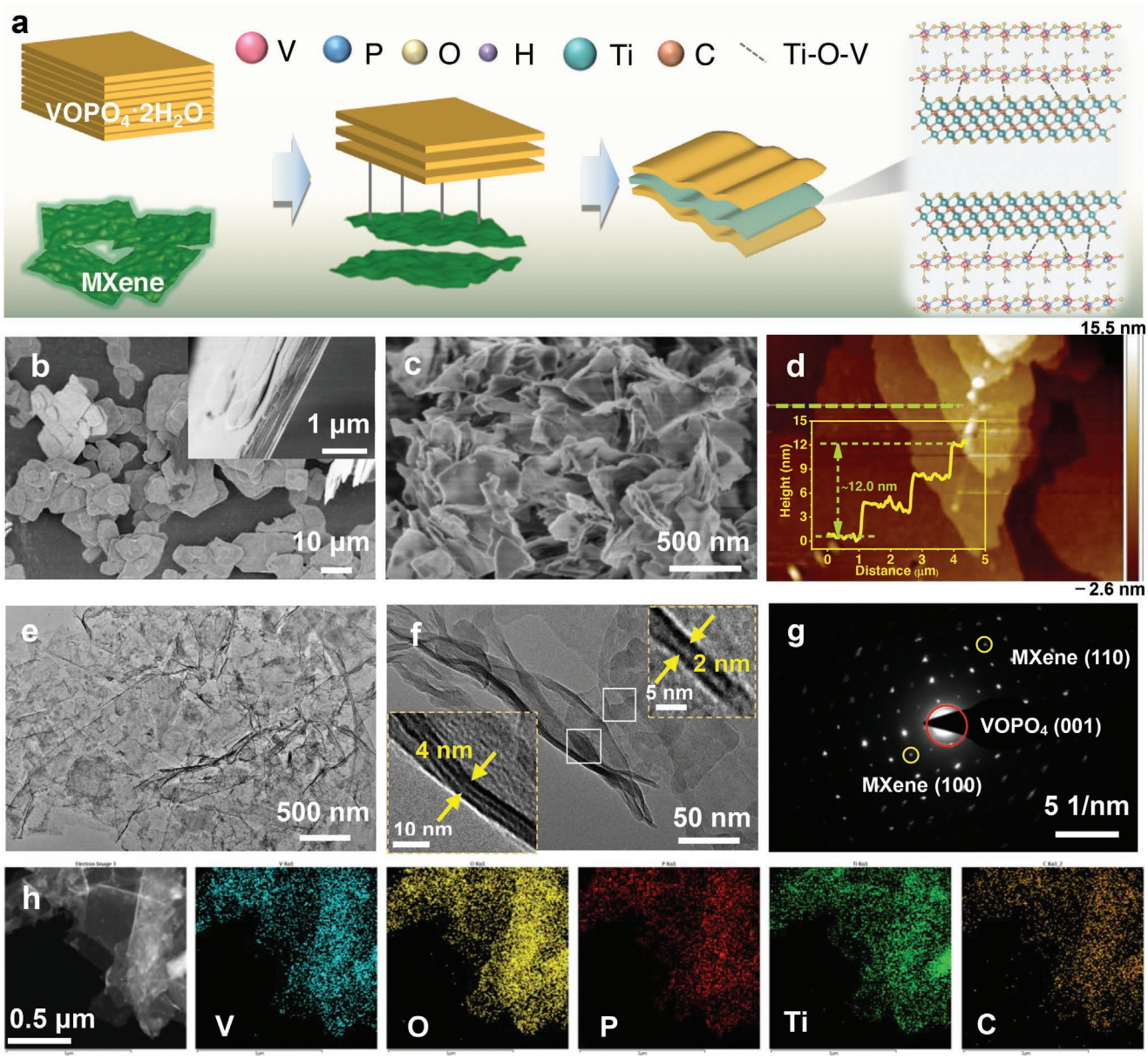

Figure 3. a) Schematic illustration for the fabrication of $VOPO_4{\cdot}nH_2O$@MXene composite. b) The SEM image of bulk $VOPO_4{\cdot}2H_2O$ (inset: the enlarged SEM image). c) SEM and d) AFM images of $VOPO_4{\cdot}nH_2O$@MXene-12 (inset: the typical height curve of the nanosheets). e) TEM and f) HRTEM images of $VOPO_4{\cdot}nH_2O$@MXene-12. g) The SAED image of $VOPO_4{\cdot}nH_2O$@MXene-12. h) STEM-EDX elemental mapping images for $VOPO_4{\cdot}nH_2O$@MXene-12.

The FTIR spectra of the $VOPO_4{\cdot}2H_2O$ and $VOPO_4{\cdot}H_2O$@MXene are presented in Figure 4b. The peaks at 1089, 971, 682, and 571 cm^{-1} are assigned to P—O extension vibration, V—O (of V=O)/V=O stretching vibration modes, V—O—P, and O—P—O bending vibrations of $VOPO_4{\cdot}2H_2O$, respectively.[11d,24] Upon hybridization with MXene, the P—O shifts to lower wavenumber, which can be ascribed to the partial reduction of V^{5+} to V^{4+}, resulting in the change of the P—O bond in the PO_4 group.[11d] Besides, the bending vibration peaks of interlayer water of $VOPO_4{\cdot}2H_2O$ and $VOPO_4{\cdot}H_2O$@MXene appear at 1613 and 1629 cm^{-1}, respectively. The blueshift of the latter suggests that the interlayer water molecules are bound solidly in the $VOPO_4{\cdot}H_2O$@MXene, leading to the improved water stability.[25] The TGA curves further confirm the water stability of the composite. As presented in Figure 4c, compared with the $VOPO_4{\cdot}2H_2O$, the incorporation of MXene increases the dehydration temperature of $VOPO_4{\cdot}H_2O$@MXene. The similar water loss hysteresis phenomena of $VOPO_4{\cdot}nH_2O$@MXene-10, $VOPO_4{\cdot}nH_2O$@MXene-16, and $VOPO_4{\cdot}nH_2O$@MXene-48 are displayed in Figure S15 (Supporting Information). Besides, the $VOPO_4{\cdot}H_2O$@MXene also displays superb insulation from the environmental water, which is witnessed by its XRD pattern

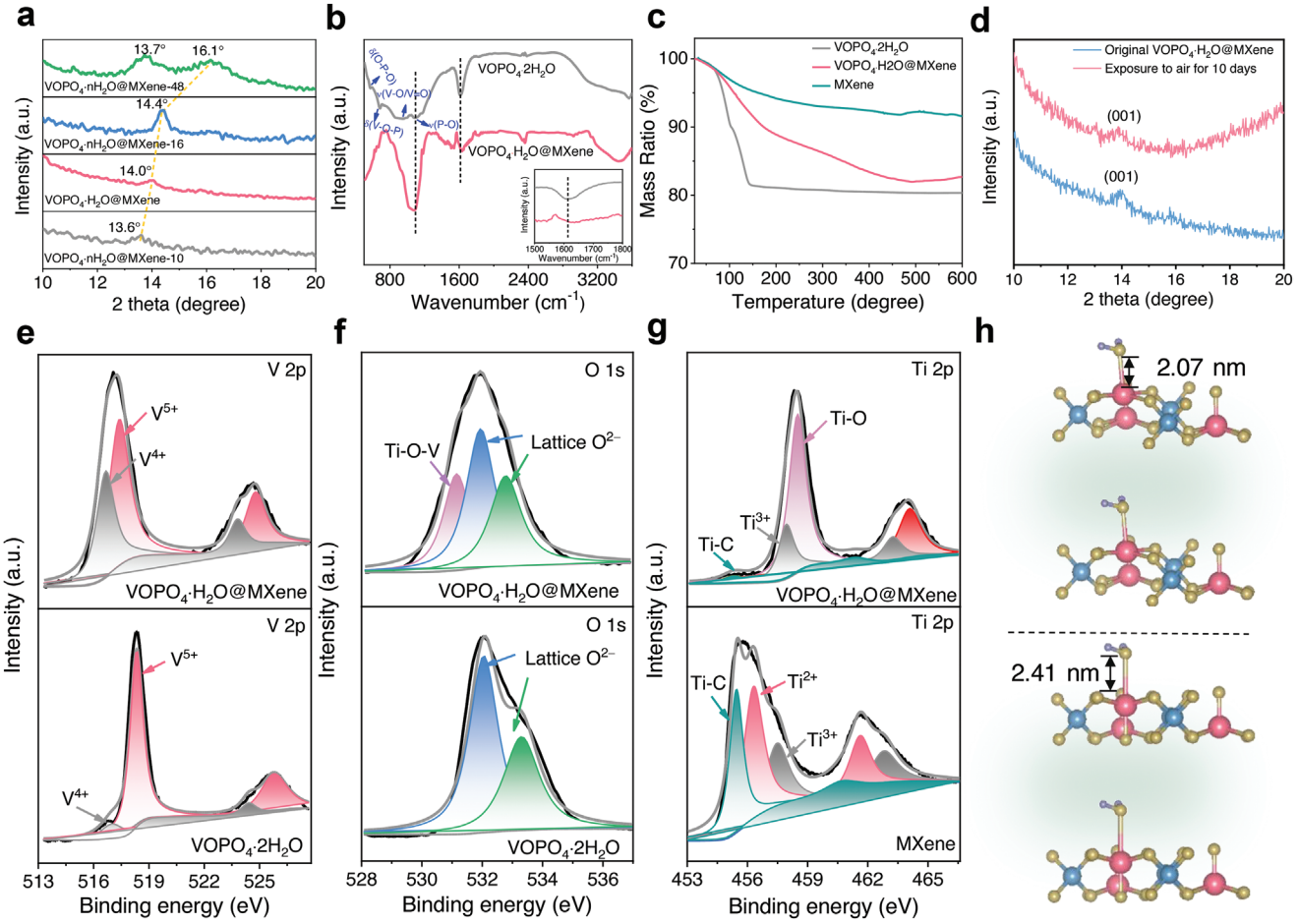

Figure 4. a) The XRD patterns of $VOPO_4{\cdot}nH_2O$@MXene-10, $VOPO_4{\cdot}nH_2O$@MXene-12 (denoted as $VOPO_4{\cdot}H_2O$@MXene), $VOPO_4{\cdot}nH_2O$@MXene-16, and $VOPO_4{\cdot}nH_2O$@MXene-48, respectively. b) The FTIR spectra of $VOPO_4{\cdot}2H_2O$ and $VOPO_4{\cdot}H_2O$@MXene (inset: enlarged view of the interlayer water characteristic peak). c) The TGA curves. d) The XRD patterns of $VOPO_4{\cdot}H_2O$@MXene before and after exposure to air. The comparison of high-resolution XPS of e) V 2p, f) O 1s for $VOPO_4{\cdot}H_2O$@MXene and $VOPO_4{\cdot}2H_2O$, and g) Ti 2p for $VOPO_4{\cdot}H_2O$@MXene and MXene. h) The calculated $V{-}O_{water}$ bond length of oxygen deficient and perfect $VOPO_4{\cdot}H_2O$.

with ignored (001) peak position shift after exposure to air for 10 days (Figure 4d). However, the $VOPO_4{\cdot}H_2O$ displays strong water adsorption ability, which can convert to $VOPO_4{\cdot}2H_2O$ in 2 min once it was exposed to air (Figure S16, Supporting Information). The excellent antiself-discharge ability and high chemical stability endow the $VOPO_4{\cdot}H_2O$@MXene with significant advantages for practical applications. Furthermore, we conducted the XPS measurement to analyze the electronic structure of $VOPO_4{\cdot}H_2O$@MXene. The full survey XPS spectrum of $VOPO_4{\cdot}H_2O$@MXene shown in Figure S17 (Supporting Information) reveals the existence of V, O, P, Ti, C, and F. Figure 4e exhibits the corresponding high-resolution XPS (HR-XPS) spectra of V 2p for $VOPO_4{\cdot}H_2O$@MXene and $VOPO_4{\cdot}2H_2O$, respectively. For $VOPO_4{\cdot}2H_2O$, the characteristic peaks at 518.3 and 525.8 eV originate from V $2p_{3/2}$ and V $2p_{1/2}$ of V^{5+}, and the peaks at 517.0 and 524.4 eV are pointed to V $2p_{3/2}$ and V $2p_{1/2}$ of V^{4+}, respectively. The amount of V^{4+} is low in this sample and most of V species exist as V^{5+}. While for $VOPO_4{\cdot}H_2O$@MXene composite, the amount of V^{4+} significantly increases, which could be attributed to the introduction of oxygen vacancies during MXene aided stripping process.[26] Moreover, the binding energies of V 2p for $VOPO_4{\cdot}H_2O$@MXene hybrid exhibit slight negative shifts, while those of Ti 2p for $VOPO_4{\cdot}H_2O$@MXene show positive shifts compared with the pure MXene (Figure 4g). These observations support the electrons transfer from conductive MXene to $VOPO_4{\cdot}H_2O$,[27] meaning a strong coupling between $VOPO_4{\cdot}H_2O$ and MXene interfaces, which is directly confirmed by the appearance of Ti—O—V in the O 1s HR-XPS spectrum of $VOPO_4{\cdot}H_2O$@MXene in comparison with that of bare $VOPO_4{\cdot}2H_2O$ (Figure 4f).[28] Additionally, the P 2p HR-XPS spectrum is given in Figure S18 (Supporting Information). In order to explore the reason behind the excellent water stability of $VOPO_4{\cdot}H_2O$@MXene, DFT calculation was carried out to compare the $V{-}O_{water}$ bond length of oxygen deficient and perfect $VOPO_4{\cdot}H_2O$, which is the quantitative index of the interaction between water molecules and $VOPO_4$. Notably, the $V{-}O_{water}$ bond length for the oxygen deficient $VOPO_4{\cdot}H_2O$ is 2.07 Å, which is 0.34 Å shorter than that for the perfect one (Figure 4h). The short bond length is indicative of strong bonding interaction between the water molecules and the $VOPO_4$, which can effectively resist water escape originating from the $V{-}O_{water}$ bonds breaking during repeated Al^{3+}

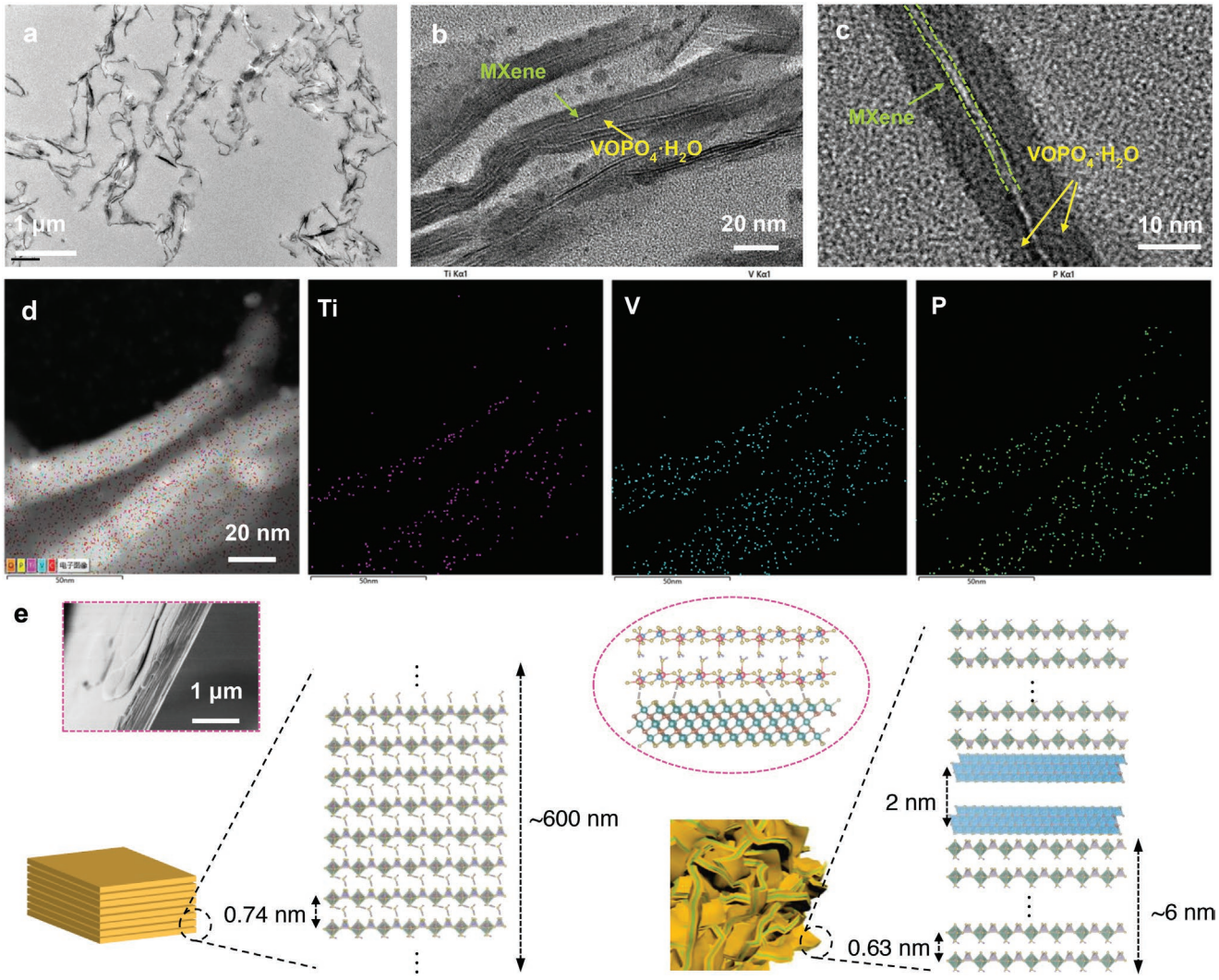

Figure 5. a) Cross-section TEM and b,c) HRTEM images of $VOPO_4 \cdot H_2O$@MXene. d) STEM-EDX elemental mapping images for $VOPO_4 \cdot H_2O$@MXene. e) Schematic illustration of the different restacking and interlayer distances of bulk $VOPO_4 \cdot 2H_2O$ and $VOPO_4 \cdot H_2O$@MXene.

insertion/deinsertion process and is beneficial to the cycling stability of the composites.

The cross-section TEM was further conducted to acquire more detailed morphology information of $VOPO_4 \cdot H_2O$@MXene. The TEM image of $VOPO_4 \cdot H_2O$@MXene exhibits uniform flexible layered structure with ultrathin feature (**Figure 5**a). The corresponding HRTEM images (Figure 5b,c) reveal that these layers are typical sandwich structures, of which the ultrathin MXene nanosheets are sandwiched between the $VOPO_4 \cdot H_2O$ nanosheets locating on both sides. Notably, the scanning transmission electron microscopy (STEM) image with energy-dispersive X-ray spectroscopy (EDS) mappings in Figure 5d; and Figure S19 (Supporting Information) present that Ti is concentrated in the central core and V and P elements are mainly distributed in the periphery, vividly corroborating the sandwich structure of $VOPO_4 \cdot nH_2O$@MXene. To sum up, the thick bulk $VOPO_4 \cdot 2H_2O$ (≈600 nm) was effectively stripped into ultrathin $VOPO_4 \cdot H_2O$ (≈6 nm) with the aid of MXene, resulting in typical sandwich structure of two MXene layers confined between the several $VOPO_4 \cdot H_2O$ nanosheets, further confirming the tight interaction between the MXene and $VOPO_4 \cdot H_2O$ (Figure 5e).

To evaluate the electrochemical performance of the $VOPO_4 \cdot H_2O$@MXene, CV curves were first recorded (**Figure 6**a). There are four pairs of reversible redox peaks at 1.95/2.14, 1.77/1.95, 1.47/1.80, and 1.18/1.51 V, respectively, which can be observed more clearly from the CV curves obtained at different scan rates (Figure S20, Supporting Information). The presence of multiple peaks demonstrates stepwise and multiple electrons transfer during the Al^{3+}insertion/deinsertion process. To further reveal the effect of the MXene amounts on the electrochemical performance, the comparison of the long-term cycling behaviors of these $VOPO_4 \cdot nH_2O$@MXene composites at the current density of 1.0 A g^{-1} in a potential window of 0.6–2.4 V is shown in Figure 6b. Remarkably, the $VOPO_4 \cdot H_2O$@MXene exhibits the most outstanding cycling

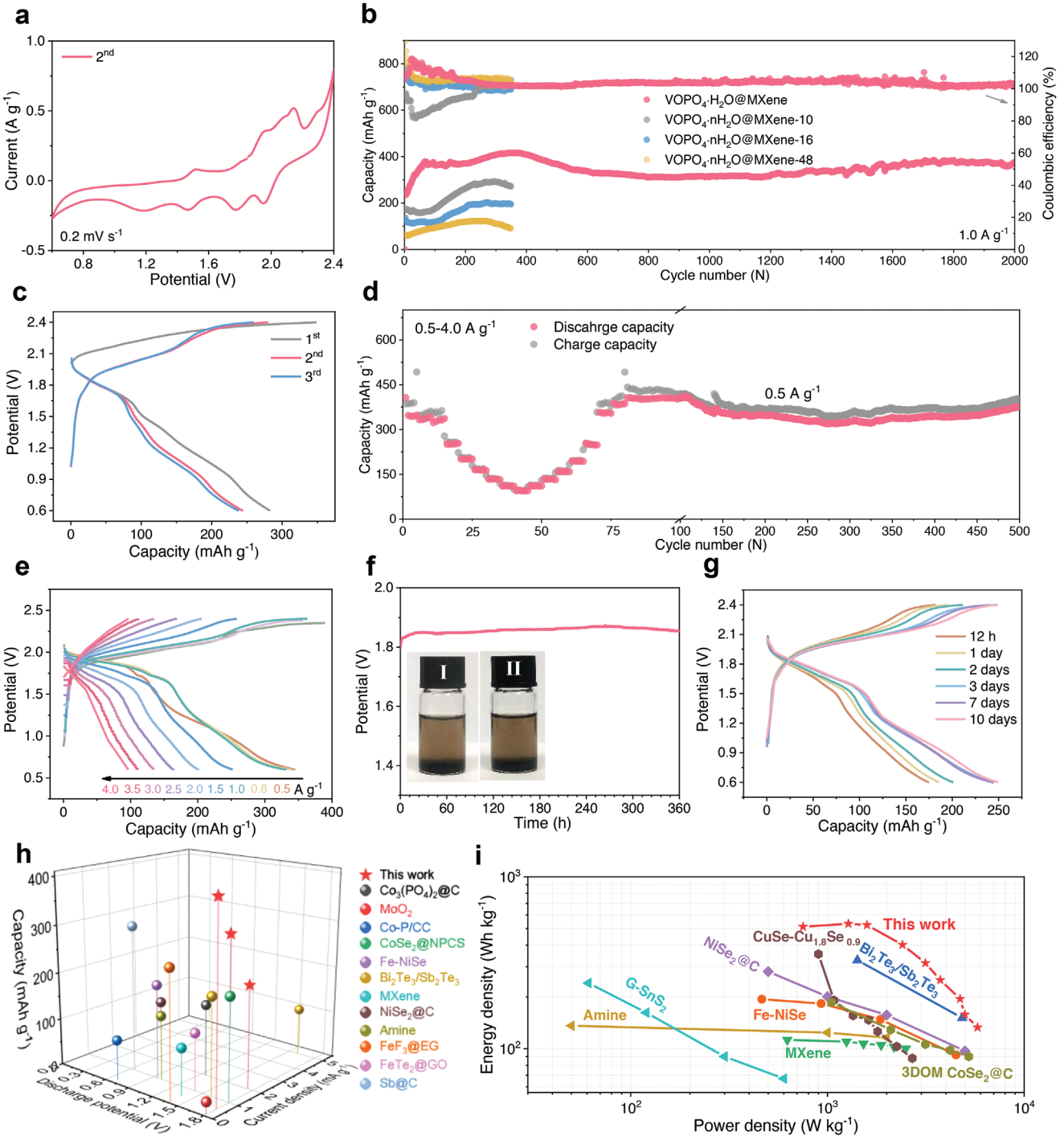

Figure 6. a) CV curves of $VOPO_4{\cdot}H_2O$@MXene cathode at 0.2 mV s^{-1}. b) Cycling performance of different $VOPO_4{\cdot}nH_2O$@MXene cathodes at a current density of 1.0 A g^{-1}. c) The initial three galvanostatic discharge/charge curves of $VOPO_4{\cdot}H_2O$@MXene at 1.0 A g^{-1}. d) The rate performance and e) galvanostatic discharge/charge voltage profiles of $VOPO_4{\cdot}H_2O$@MXene cathode at different current densities. f) OCV and g) capacity retention tests of $VOPO_4{\cdot}H_2O$@MXene cathode (inset: digital images of $VOPO_4{\cdot}H_2O$@MXene soaked in ionic liquid electrolyte (I) before and (II) after 2 months). h) Electrochemical performance comparison of $VOPO_4{\cdot}H_2O$@MXene with the recently reported advanced AIBs cathodes. i) Ragone plots of $VOPO_4{\cdot}H_2O$@MXene and other representative AIBs cathodes.

performance, which affords an initial discharge capacity of 282.5 mAh g^{-1} and undergoes a moderately augmenting capacity up to 416.6 mAh g^{-1} at the 349th cycle and maintains the capacity of 374.8 mAh g^{-1} over 2000 cycles. It also delivers high reversible Al^{3+} storage property with the average Coulombic efficiency of ≈100% among the whole cycles. Clearly, this is due to the suitable water content in this composite. The gradual discharge capacity increment could be ascribed to the exfoliation

of some thick nanosheets during the continuous intercalation/deintercalation of Al^{3+} ions, providing more active sites for Al^{3+} ions storage as well as shortening ions diffusion length.[29] The similar phenomenon was observed in some previous reported 2D cathode materials for AIBs.[30] The structural evolution is confirmed by the XRD pattern of $VOPO_4 \cdot H_2O$@MXene after cycling. As displayed in Figure S21 (Supporting Information), the (001) characteristic peak for $VOPO_4 \cdot H_2O$ disappears after repeated Al^{3+} ions intercalation/deintercalation. This peak response might be related to the exfoliation of the nanosheets during cycling, which corresponds well with the increased capacity. Moreover, the XPS spectra of the cycled $VOPO_4 \cdot H_2O$@MXene remain almost unchanged (Figure S22, Supporting Information), which proves the good stability of the electrode during the cycling process. The corresponding galvanostatic charge/discharge curves of $VOPO_4 \cdot H_2O$@MXene given in Figure 6c present desirable high discharge/charge potentials of around 1.8/2.0 V, indicative of potential high energy density of the $VOPO_4 \cdot H_2O$@MXene. In addition, the discharge/charge curves can be well maintained, confirming its superior stability. The galvanostatic discharge/charge curves of $VOPO_4 \cdot nH_2O$@MXene-10, $VOPO_4 \cdot nH_2O$@MXene-16, and $VOPO_4 \cdot nH_2O$@MXene-48 provided in Figure S23 (Supporting Information) showcase similar voltage plateaus with $VOPO_4 \cdot H_2O$@MXene. Besides excellent cycle life, a fast Al^{3+} ions storage/release is another requirement of the promising AIBs. Figure 6d displays the galvanostatic rate performance of the $VOPO_4 \cdot H_2O$@MXene cathode. It shows exceptionally high rate capability, with average reversible capacities of 355.7, 336.4, 329.8, 251.6, 200.9, 164.2, 133.4, 110.8, and 94.4 mAh g^{-1} at applied current densities of 0.5, 0.8, 1.0, 1.5, 2.0, 2.5, 3.0, 3.5, and 4.0 A g^{-1}, respectively. Noting that the observed rate capability is comparable, or superior, to the state-of-the-art reported AIBs cathodes previously (Figure S24, Supporting Information).[30a,31] The good rate performance could be credited to the function of $VOPO_4 \cdot H_2O$ with advanced Al^{3+} storage properties along with the good electronic conductivity provided by the MXene. As shown in Figure S25 (Supporting Information), the density of states (DOS) for $VOPO_4 \cdot H_2O$@MXene and $VOPO_4 \cdot H_2O$ was calculated, as a major determining factor of the electronic conductivity of inorganic materials. As expected, the $VOPO_4 \cdot H_2O$@MXene shows the stronger metallic character because of the continuous electronic state at Fermi level, and enhanced DOS intensity compared to that of $VOPO_4 \cdot H_2O$, suggesting that the incorporated MXene is beneficial for modulating and ameliorating the conductivity.[32] When the current density is reverted to 0.5 A g^{-1}, the $VOPO_4 \cdot H_2O$@MXene affords a higher discharge capacity of 404.9 mAh g^{-1}. This phenomenon is attributed to gradual activation of the cathode and the exposure of active sites for Al^{3+} intercalation during the rate cycling. Somewhat surprisingly, after the high rate testing, the cathode still delivers steady capacity of 404.5 mAh g^{-1} at 0.5 A g^{-1} after 420 cycles (Figure 6d). Besides, the corresponding discharge/charge profiles at different current rates given in Figure 6e display discernible discharge/charge plateaus. To further prove the superiority of the $VOPO_4 \cdot H_2O$@MXene cathode, the long-term cyclability at a high current density of 2 A g^{-1} is checked and manifested in Figure S26 (Supporting Information). The $VOPO_4 \cdot H_2O$@MXene achieves a discharge capacity of 130.3 mAh g^{-1} for the 1st cycle and affords the capacity of 214.1 mAh g^{-1} even after 2000 cycles, confirming its extraordinary cycling stability. The excellent cycling results offer solid evidence for the high water-holding ability of $VOPO_4 \cdot H_2O$@MXene, which ensures smooth Al^{3+} ions diffusion kinetics and high structural stability. To further verify the intrinsic advanced characters of the $VOPO_4 \cdot H_2O$@MXene, the self-discharging investigation and static electrolyte soaking test were conducted. For the self-discharging test, the OCV value of the $VOPO_4 \cdot H_2O$@MXene keeps consistent within 15 days (Figure 6f). Besides, we placed the fully charged $VOPO_4 \cdot H_2O$@MXene battery at OCV for specific time (0.5–10 days), and then the battery was fully discharged at 1.0 A g^{-1}. Remarkably, instead of falling, the discharge capacity of $VOPO_4 \cdot H_2O$@MXene increased after 10 days, demonstrating its excellent antiself-discharge ability (Figure 6g). Additionally, the $VOPO_4 \cdot H_2O$@MXene remains unchanged even after 60 days' immersion treatment, indicating its outstanding chemical stability in the highly acidic electrolyte (inset in Figure 6f). Moreover, the TGA test was further conducted to check the water stability of $VOPO_4 \cdot H_2O$@MXene during cycling process (Figure S27, Supporting Information). The cycled cathode shows a similar weight loss trend compared with bare $VOPO_4 \cdot H_2O$@MXene, except for larger weight loss at high temperature, which can be ascribed to the PVDF decomposition.[33] The calculated water content (after subtracting the PDVF content) in cycled $VOPO_4 \cdot H_2O$@MXene is around 17%, which is close to that in the pristine one (18%), confirming its high water stability originating from the fixation effect of MXene. To the best of our knowledge, such high-level performances of $VOPO_4 \cdot H_2O$@MXene, including the large reversible discharge capacities obtained at high current densities and elevated operating voltage, are among the best one in the reported cathode materials for AIBs (Figure 6h; and Table S2, Supporting Information).[7,31a,b,d,i,34] The corresponding Ragone plot in Figure 6i shows that $VOPO_4 \cdot H_2O$@MXene stands out in terms of both energy density (533 Wh kg^{-1}) and power density (5792 W kg^{-1}) calculated from the corrected capacities (Figures S28 and S29, Supporting Information), owing to its high discharge voltage plateau and rate capability among these previously reported AIBs cathodes.[31a–d,h,34c,d,35]

A closer look of the electrode kinetics is realized by CV measurements performed at different sweep rates. As exhibited in Figure S30a (Supporting Information), the redox peaks in CV curves gradually expand with the increasing sweep rates. The cathodic current peaks can be observed at all sweep rates, while the high-potential anodic current peaks tend to be blurry because of the increased Ohmic losses at high sweep rates. To discern the charge storage process of $VOPO_4 \cdot H_2O$@MXene, the peak currents and their corresponding sweep rates should obey the power law expression and the exponent can be determined by fitting the cathodic and anodic current peaks at around 1.7/1.8 and 1.9 V, respectively. The power law relationship is described by

$$i = av^b \quad (1)$$

where i represents the measured peak current, v is the scan rate, and a and b are fitting parameters. The b value can be used

to identify between diffusion-controlled and surface-controlled contributions, i.e., $b = 0.5$ is regarded a pure Faradaic process and $b = 1$ is a pure capacitive process.[36] The calculated b values shown in Figure S30b (Supporting Information) for these cathode and anode peaks are 0.87 (peak I), 1.10 (peak II), 0.75 (peak III), respectively, suggestive of a capacitance-controlled process, which facilitates Al^{3+} diffusion kinetics and enables the high rate capability of $VOPO_4 \cdot H_2O$@MXene. Such pseudocapacitive storage endows the cathode with high energy and power densities.

3. Conclusions

In summary, we creatively raise and confirm the positive role of the water molecules for enhancing the AIBs performance employing $VOPO_4 \cdot nH_2O$ (n = 0, 1, 2) as research models. Both of the oxygen anion and vanadium cation participate in the charge compensation when the Al^{3+} ions intercalate into the hydrate. Benefiting from the Al^{3+} charge shielding role of water molecules and smaller steric hindrance, the $VOPO_4 \cdot H_2O$ delivers the highest reversible capacity and fastest Al^{3+} migration compared with $VOPO_4$ and $VOPO_4 \cdot 2H_2O$. Additionally, we also attest that the main reason for the cycling instability for the hydrate is the irreversible water loss. Consequently, a novel strategy to obtain $VOPO_4 \cdot H_2O$ with high water stability was developed through a simple stirring of $VOPO_4 \cdot 2H_2O$ and MXene. The $VOPO_4 \cdot H_2O$@MXene delivers high reversible capacity (329.6 mAh g^{-1} at 1 A g^{-1}), long and high discharge plateau (≈1.8 V), high energy density, and encouraging cycling life (2000 cycles at 1 A g^{-1} and 2000 cycles at 2 A g^{-1} without capacity loss). This finding not only provides novel alternative of the high-performance cathode materials in AIBs, but also presents a new insight into cathode design.

Supporting Information

Supporting Information is available from the Wiley Online Library or from the author.

Acknowledgements

This work was supported by the National Natural Science Foundation of China (No. 51971065), and the Innovation Program of Shanghai Municipal Education Commission (No. 2019-01-07-00-07). The authors would like to thank SCI-GO (www.sci-go.com) for the XPS analysis.

Conflict of Interest

The authors declare no conflict of interest.

Data Availability Statement

The data that support the findings of this study are available in the supplementary material of this article.

Keywords

aluminum ion batteries, high discharge potential, high water stability, $VOPO_4 \cdot H_2O$, $VOPO_4 \cdot H_2O$@MXene

Received: December 7, 2022
Revised: January 29, 2023
Published online: February 12, 2023

[1] J. W. Choi, D. Aurbach, *Nat. Rev. Mater.* **2016**, *1*, 16013.
[2] a) Y. Liang, H. Dong, D. Aurbach, Y. Yao, *Nat. Energy* **2020**, *5*, 646; b) A. Ponrouch, J. Bitenc, R. Dominko, N. Lindahl, P. Johansson, M. R. Palacin, *Energy Storage Mater.* **2019**, *20*, 253.
[3] a) S. K. Das, *Angew. Chem., Int. Ed.* **2018**, *57*, 16606; b) A. L. Jadhav, J. H. Xu, R. J. Messinger, *ACS Energy Lett.* **2020**, *5*, 2842.
[4] M.-C. Lin, M. Gong, B. Lu, Y. Wu, D.-Y. Wang, M. Guan, M. Angell, C. Chen, J. Yang, B.-J. Hwang, H. Dai, *Nature* **2015**, *520*, 324.
[5] W. Kaveevivitchai, A. J. Jacobson, *Chem. Mater.* **2016**, *28*, 4593.
[6] M. Chiku, H. Takeda, S. Matsumura, E. Higuchi, H. Inoue, *ACS Appl. Mater. Interfaces* **2015**, *7*, 24385.
[7] J. Wei, W. Chen, D. Chen, K. Yang, *J. Electrochem. Soc.* **2017**, *164*, A2304.
[8] S. Wang, K. V. Kravchyk, S. Pigeot-Rémy, W. Tang, F. Krumeich, M. Wörle, M. I. Bodnarchuk, S. Cassaignon, O. Durupthy, S. Zhao, C. Sanchez, M. V. Kovalenko, *ACS Appl. Nano Mater.* **2019**, *2*, 6428.
[9] C. Legein, B. J. Morgan, F. Fayon, T. Koketsu, J. Ma, M. Body, V. Sarou-Kanian, X.-K. Wei, M. Heggen, O. J. Borkiewicz, P. Strasser, D. Dambournet, *Angew. Chem., Int. Ed.* **2020**, *59*, 19247.
[10] a) E. Levi, Y. Gofer, D. Aurbach, *Chem. Mater.* **2010**, *22*, 860; b) P. Novák, W. Scheifele, F. Joho, O. Haas, *J. Electrochem. Soc.* **1995**, *142*, 2544.
[11] a) B. M. Azmi, T. Ishihara, H. Nishiguchi, Y. Takita, *J. Power Sources* **2003**, *119–121*, 273; b) G. He, W. H. Kan, A. Manthiram, *Chem. Mater.* **2016**, *28*, 682; c) J. Hyoung, J. W. Heo, M. S. Chae, S.-T. Hong, *ChemSusChem* **2019**, *12*, 1069; d) V. Verma, S. Kumar, W. Manalastas, J. Zhao, R. Chua, S. Meng, P. Kidkhunthod, M. Srinivasan, *ACS Appl. Energy Mater.* **2019**, *2*, 8667; e) X. Ji, J. Chen, F. Wang, W. Sun, Y. Ruan, L. Miao, J. Jiang, C. Wang, *Nano Lett.* **2018**, *18*, 6441; f) P. Xiong, F. Zhang, X. Zhang, S. Wang, H. Liu, B. Sun, J. Zhang, Y. Sun, R. Ma, Y. Bando, C. Zhou, Z. Liu, T. Sasaki, G. Wang, *Nat. Commun.* **2020**, *11*, 3297.
[12] F. Wang, W. Sun, Z. Shadike, E. Hu, X. Ji, T. Gao, X.-Q. Yang, K. Xu, C. Wang, *Angew. Chem., Int. Ed.* **2018**, *57*, 11978.
[13] a) J. Zheng, S. Ju, L. Yao, G. Xia, X. Yu, *J. Power Sources* **2021**, *511*, 230450; b) H. Shao, K. Xu, Y.-C. Wu, A. Iadecola, L. Liu, H. Ma, L. Qu, E. Raymundo-Piñero, J. Zhu, Z. Lin, P.-L. Taberna, P. Simon, *ACS Energy Lett.* **2020**, *5*, 2873; c) P. Yan, L. Ji, X. Liu, Q. Guan, J. Guo, Y. Shen, H. Zhang, W. Wei, X. Cui, Q. Xu, *Nano Energy* **2021**, *86*, 106139.
[14] M. H. Alfaruqi, V. Mathew, J. Song, S. Kim, S. Islam, D. T. Pham, J. Jo, S. Kim, J. P. Baboo, Z. Xiu, K.-S. Lee, Y.-K. Sun, J. Kim, *Chem. Mater.* **2017**, *29*, 1684.
[15] a) J. Wang, S. Tan, F. Xiong, R. Yu, P. Wu, L. Cui, Q. An, *Chem. Commun.* **2020**, *56*, 3805; b) Y. Xu, X. Wu, S. K. Sandstrom, J. J. Hong, H. Jiang, X. Chen, X. Ji, *Adv. Mater.* **2021**, *33*, 2105234.
[16] K. Li, Y. Li, Z. Xie, X. Tan, X. Zhang, R. Liu, Y.-F. Song, S. Zhang, *ACS Appl. Nano Mater.* **2021**, *4*, 2503.
[17] F. Wan, Y. Zhang, L. Zhang, D. Liu, C. Wang, L. Song, Z. Niu, J. Chen, *Angew. Chem., Int. Ed.* **2019**, *58*, 7062.
[18] S. Saha, G. Assat, M. T. Sougrati, D. Foix, H. Li, J. Vergnet, S. Turi, Y. Ha, W. Yang, J. Cabana, G. Rousse, A. M. Abakumov, J.-M. Tarascon, *Nat. Energy* **2019**, *4*, 977.

[19] R. Gautier, N. Audebrand, E. Furet, R. Gautier, E. L. Fur, *Inorg. Chem.* **2011**, *50*, 4378.
[20] J. Wang, J. Wang, Y. Jiang, F. Xiong, S. Tan, F. Qiao, J. Chen, Q. An, L. Mai, *Adv. Funct. Mater.* **2022**, *32*, 2113030.
[21] F. Wu, H. Yang, Y. Bai, C. Wu, *Adv. Mater.* **2019**, *31*, 1806510.
[22] K. Nasrin, V. Sudharshan, K. Subramani, M. Karnan, M. Sathish, *Small* **2022**, *18*, 2106051.
[23] a) Y. Zhu, L. Peng, D. Chen, G. Yu, *Nano Lett.* **2016**, *16*, 742; b) H. Li, L. Peng, Y. Zhu, D. Chen, X. Zhang, G. Yu, *Energy Environ. Sci.* **2016**, *9*, 3399.
[24] L. Hu, Z. Wu, C. Lu, F. Ye, Q. Liu, Z. Sun, *Energy Environ. Sci.* **2021**, *14*, 4095.
[25] J. Xie, Z. Liang, Y.-C. Lu, *Nat. Mater.* **2020**, *19*, 1006.
[26] Z. Wu, C. Lu, F. Ye, L. Zhang, L. Jiang, Q. Liu, H. Dong, Z. Sun, L. Hu, *Adv. Funct. Mater.* **2021**, *31*, 2106816.
[27] a) H. Wang, K. Xie, Y. You, Q. Hou, K. Zhang, N. Li, W. Yu, K. P. Loh, C. Shen, B. Wei, *Adv. Energy Mater.* **2019**, *9*, 1901806; b) Q. Pan, Q. Zhang, F. Zheng, Y. Liu, Y. Li, X. Ou, X. Xiong, C. Yang, M. Liu, *ACS Nano* **2018**, *12*, 12578.
[28] H. Liu, P. He, J. Cao, T. Duan, Q. Kong, W. Yao, *J. Power Sources* **2022**, *521*, 230946.
[29] J. Tang, X. Huang, T. Lin, T. Qiu, H. Huang, X. Zhu, Q. Gu, B. Luo, L. Wang, *Energy Storage Mater.* **2020**, *26*, 550.
[30] a) L. Xing, K. A. Owusu, X. Liu, J. Meng, K. Wang, Q. An, L. Mai, *Nano Energy* **2021**, *79*, 105384; b) S. Guo, H. Yang, M. Liu, X. Feng, H. Xu, Y. Bai, C. Wu, *ACS Appl. Energy Mater.* **2021**, *4*, 7064; c) X. Huo, B. Zhang, J. Li, X. Wang, T. Qin, Y. Zhang, F. Kang, *ACS Appl. Mater. Interfaces* **2021**, *13*, 11822; d) X. Feng, J. Li, Y. Ma, C. Yang, S. Zhang, J. Li, C. An, *ACS Appl. Energy Mater.* **2021**, *4*, 1575.
[31] a) H. Lu, Y. Li, Y. Zheng, C. Dong, Y. Li, F. Meng, Y. Wang, C. Teng, X. Wang, D. Zhou, G. Xue, *Mater. Today Energy* **2022**, *24*, 100940; b) H. Zhang, Y. Liu, L. Yang, L. Zhao, X. Dong, H. Wang, Y. Li, T. Sun, Q. Li, H. Li, *Energy Storage Mater.* **2022**, *47*, 336; c) H. Hong, J. Liu, H. Huang, C. Atangana Etogo, X. Yang, B. Guan, L. Zhang, *J. Am. Chem. Soc.* **2019**, *141*, 14764; d) G. Wang, E. Dmitrieva, B. Kohn, U. Scheler, Y. Liu, V. Tkachova, L. Yang, Y. Fu, J. Ma, P. Zhang, F. Wang, J. Ge, X. Feng, *Angew. Chem., Int. Ed.* **2022**, *61*, e202116194; e) D.-J. Yoo, M. Heeney, F. Glöcklhofer, J. W. Choi, *Nat. Commun.* **2021**, *12*, 2386; f) X. Peng, Y. Xie, A. Baktash, J. Tang, T. Lin, X. Huang, Y. Hu, Z. Jia, D. J. Searles, Y. Yamauchi, L. Wang, B. Luo, *Angew. Chem., Int. Ed.* **2022**, *61*, e202203646; g) Z. Zhao, Z. Hu, Q. Li, H. Li, X. Zhang, Y. Zhuang, F. Wang, G. Yu, *Nano Today* **2020**, *32*, 100870; h) X. Li, W. Lv, G. Wu, G. Fu, W. Zhang, Z. Li, *Chem. Eng. J.* **2021**, *426*, 131899; i) C. Li, S. Dong, P. Wang, C. Wang, L. Yin, *Adv. Energy Mater.* **2019**, *9*, 1902352.
[32] S. Das, P. Bhauriyal, B. Pathak, *J. Phys. Chem. C* **2021**, *125*, 49.
[33] S. H. Siyal, S. S. A. Shah, T. Najam, M. S. Javed, M. Imran, J.-L. Lan, *ACS Appl. Energy Mater.* **2021**, *4*, 8604.
[34] a) S. Lu, M. Wang, F. Guo, J. Tu, A. Lv, Y. Chen, S. Jiao, *Chem. Eng. J.* **2020**, *389*, 124370; b) L. Yao, S. Ju, T. Xu, X. Yu, *ACS Nano* **2021**, *15*, 13662; c) Y. Du, B. Zhang, W. Zhang, H. Jin, J. Qin, J. Wan, J. Zhang, G. Chen, *Energy Storage Mater.* **2021**, *38*, 231; d) X. Huo, J. Zhong, Z. Yang, J. Feng, J. Li, F. Kang, *ACS Appl. Mater. Interfaces* **2021**, *13*, 55112; e) J. Zhang, L. Zhang, Y. Zhao, J. Meng, B. Wen, K. M. Muttaqi, M. R. Islam, Q. Cai, S. Zhang, *Adv. Energy Mater.* **2022**, *12*, 2200959; f) L. Yang, J. Liu, Y. Liu, Y. Li, Y. Xu, F. Zuo, Y. Wu, Q. Li, H. Li, *Chem. Commun.* **2022**, *58*, 10981; g) T. Li, H. Hu, T. Cai, X. Liu, Y. Wang, L. Wang, Y. Zhang, W. Xing, Z. Yan, *Nanoscale* **2022**, *14*, 10566.
[35] Y. Hu, B. Luo, D. Ye, X. Zhu, M. Lyu, L. Wang, *Adv. Mater.* **2017**, *29*, 1606132.
[36] H. Lindström, S. Södergren, A. Solbrand, H. Rensmo, J. Hjelm, A. Hagfeldt, S.-E. Lindquist, *J. Phys. Chem. B* **1997**, *101*, 7717.